

Article

The Effects of Iron-Bearing Intermetallics on the Fitness-for-Service Performance of a Rare-Earth-Modified A356 Alloy for Next Generation Automotive Powertrains

Joshua Stroh ^{1,*}, Dimitry Sediako ¹  and David Weiss ²

¹ High Performance Powertrain Materials Laboratory, School of Engineering, The University of British Columbia–Okanagan, 1137 Alumni Ave, Kelowna, BC V1V 1V7, Canada; dimitry.sediako@ubc.ca

² Eck Industries, 1602 N 8th St., Manitowoc, WI 54220, USA; david.weiss@eckindustries.com

* Correspondence: josh_stroh@alumni.ubc.ca

Abstract: Aimed at improving the tensile strength and creep resistance of a rare earth-modified A356 alloy, this study adjusted the Mg and Mn concentration in the alloy, specifically aiming to transform the harmful Al_5FeSi and $Al_9FeSi_3Mg_5$ phase into $Al_{15}(Fe,Mn)_3Si_2$. It was found that lowering the Mg concentration from 0.49 to 0.25 wt.% and raising the Mn concentration from 0.10 to 0.41 wt.% resulted in a near complete transformation of the Fe-bearing phases. This transformation led to a greater total volume fraction of Fe-intermetallics (2.9 to 4.1%), without affecting the volume fraction of the desirable, temperature-resistant, AlSiRE phase. Moreover, the chemistry modification led to a shift in the morphology of the AlSiRE phase while reducing its size. Combined with the decreased volume fraction of the harmful Fe precipitates, the chemistry modification improved the yield strength (YS), ultimate tensile strength (UTS) and modulus of elasticity by ~14%, 9%, and 10%, respectively. In addition, the steady-state creep rates of the high Mn alloy were lower at all stresses as compared to the low Mn alloy and the fracture stress was ~15 MPa higher, reaching 100% of the alloy's original 250 °C YS.

Keywords: aluminum powertrain alloys; casting; rare earth mischmetal; creep properties; tensile properties; Mn addition; Fe phases



Citation: Stroh, J.; Sediako, D.; Weiss, D. The Effects of Iron-Bearing Intermetallics on the Fitness-for-Service Performance of a Rare-Earth-Modified A356 Alloy for Next Generation Automotive Powertrains. *Metals* **2021**, *11*, 788. <https://doi.org/10.3390/met11050788>

Academic Editor: Elisabetta Gariboldi

Received: 17 April 2021

Accepted: 11 May 2021

Published: 13 May 2021

Publisher's Note: MDPI stays neutral with regard to jurisdictional claims in published maps and institutional affiliations.



Copyright: © 2021 by the authors. Licensee MDPI, Basel, Switzerland. This article is an open access article distributed under the terms and conditions of the Creative Commons Attribution (CC BY) license (<https://creativecommons.org/licenses/by/4.0/>).

1. Introduction

The cumulative global emissions produced by the automotive industry over the last decade have put a tremendous strain on the environment. This has resulted in the implementation of stringent government legislation, set in 2012, which mandates that the corporate average fuel economy (CAFE) be increased to 54.5 miles per gallon (MPG) by the year 2025. As a reference, the CAFE in 2012 and 2017 was ~25 and ~30 MPG, respectively. It should be noted that due to slow progress, a new US efficiency standard was introduced in 2021, which proposes an increase of 1.5% per year in vehicle fuel economy from 2021 to 2026 (i.e., Safer, Affordable, Fuel-Efficient (SAFE) vehicles rule). Consequently, automotive engineers and manufacturers have made tremendous efforts toward increasing the efficiencies of their automobiles. Several methods exist for improving efficiencies, but this is typically accomplished by either weight reduction, through the use of lightweight materials, or increasing the internal operating pressure and, therefore, the temperature of the internal combustion (IC) engine. However, the currently used aluminum alloys (i.e., A356, A319, etc.) have a high tendency to weaken with increasing temperatures, limiting their practical use to applications that operate under 200–300 °C (current operating temperature of the critical engines components). Consequently, this prevents the transportation industry from increasing their operating efficiencies and reducing their carbon footprint. Thus, it is necessary to investigate new methods of improving the elevated temperature performance of aluminum (Al) alloys.

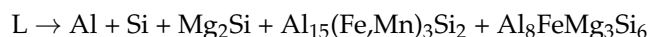
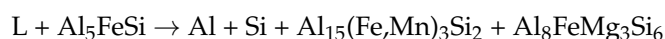
One of the methods for improving the temperature resistance of Al alloys is through the introduction of rare earth (RE) elements such as cerium (Ce) or lanthanum (La) [1–4]. Combined with Al and/or Si, these REs form several hard precipitates with great thermal stability. For example, a previous in-situ neutron diffraction solidification study performed by the authors revealed that an $\text{Al}_{11}\text{Ce}_3$ phase was still present in the AlCe alloy until $\sim 650^\circ\text{C}$ [3,4]. It should be noted that studying the effects that REs have on the microstructure and mechanical properties of Al alloys has been researched since the early 1900s [5–9]; however, these studies were restricted to ambient temperature testing of laboratory alloys, and thus their effect on the elevated temperature performance of commercial Al alloys was unknown.

Recently, E. Aghaie et al. [10] characterized the effects that small additions (0.1 to 1 wt.%) of Ce have on the room and elevated temperature mechanical properties of a commonly used powertrain alloy, B319 (Al-Si-Cu-Mg based). The study indicated that 0.1 wt.% of Ce resulted in the greatest increase in the room temperature yield strength (YS) (i.e., 150 to 165 MPa) and ultimate tensile strength (UTS) (214 to 234 MPa). In addition, at 250°C , the B319 alloy's YS and UTS improved from 110 and 139 MPa to 125 and 149 MPa, respectively. It should be noted that the alloys described in the aforementioned study were not conditioned prior to conducting the tensile test, and thus the tensile properties would likely degrade further after being exposed to an elevated temperature for an extended period of time. Jin et al. [11] reported that the yield strength, at 300°C , of a T6 heat-treated A319 alloy was reduced by $\sim 20\text{--}50\%$ (depending on alloy modification) after conditioning the alloy at the testing temperature for 100 h prior to initiating the elevated temperature tensile test. Thus, pre-subjecting the alloy to the testing temperature for 100–200 h (i.e., conditioning) prior to initiating a tensile/creep/fatigue test is essential for obtaining a realistic representation of the actual in-service performance of the alloy.

Since obtaining pure Ce metal is time- and resource-intensive, Ce is more readily available as an RE alloy called mischmetal (typically Ce and La dominant, with smaller additions of other RE elements such as neodymium (Nd) and praseodymium (Pr)). Mischmetal is considered a byproduct when mining for these RE elements, and fortunately, it is widely abundant and thus economically feasible ($\$2/\text{kg}$ for LREEs) for alloying Al alloys. Moreover, Z. Sims et al. [12] evaluated the efficacy of replacing Ce metal with RE mischmetal by comparing the mechanical properties, phase constituency, and thermal stability of aluminum alloyed with either 12 wt.% Ce or 12 wt.% RE mischmetal. They reported that the use of RE mischmetal led to a slight undercooling of the alloy, causing the formation of a few primary $\text{Al}_{11}\text{Ce}_3$ crystals, which led to a slight reduction in the alloy's ductility and ultimate tensile strength, but was accompanied by a moderate increase in the yield strength. Despite the small differences between the two alloys, the use of RE mischmetal over Ce metal is a viable option that would diversify supply chains and reduce costs for aluminum alloy producers [13]. As a result, the current authors studied the effects that a 3.5 wt.% RE addition has on the microstructure and elevated temperature tensile properties of an A356 type Al alloy [14]. It was observed that the RE addition led to a considerable increase in the alloy's yield and ultimate tensile strength at 250 and 300°C . The improvements were attributed to the development of a well-dispersed, thermally stable AlSiRE phase. Although this phase improved the tensile strength and temperature resistance of the A356 alloy, the naturally occurring iron (Fe) impurities in the A356 base material led to the formation of unwanted Fe-bearing intermetallics, specifically $\beta\text{-Al}_5\text{FeSi}$ (also reported as $\text{Al}_{4.5}\text{FeSi}$) and $\pi\text{-Al}_9\text{FeMg}_3\text{Si}_5$ (also reported as $\text{Al}_8\text{FeMg}_3\text{Si}_6$). Among the two phases, $\beta\text{-Al}_5\text{FeSi}$ has the most detrimental effect on the alloy's strength and fracture toughness [15]. The main reasons for this are that the needle-like geometry of the $\beta\text{-Al}_5\text{FeSi}$ phase acts as a stress concentrator, the phase has a large aspect ratio (high interfacial energy), and also lowers the feedability of the molten alloy during casting by blocking the interdendritic flow channels towards the end of solidification [16–18]. Insufficient feeding of the material during solidification can lead to a higher volume fraction of porosity and thus even greater magnitudes of stress concentrating. Moreover, it has been reported that

β -Al₅FeSi acts as a nucleation poisoning site, thereby leading to larger grain sizes and lower mechanical properties [19]. Fortunately, modification of the alloy's manganese (Mn) and/or magnesium (Mg) concentration can result in the transformation of these two harmful Fe-bearing intermetallics into the more morphologically favorable α -Al₁₅(Fe,Mn)₃Si₂ phase. The Chinese script or polygonal morphology of the α -Al₁₅(Fe,Mn)₃Si₂ phase lowers stress concentrations and interfacial energies and generally results in increased toughness. This transformation of β -Al₅FeSi phase into α -Al₁₅(Fe,Mn)₃Si₂ was called neutralization or iron correction in the study [18]. It has been observed that an Mn:Fe ratio as low as 0.1:1 can result in the partial transformation of β -Al₅FeSi into α -Al₁₅(Fe,Mn)₃Si₂; however, the greatest results occur near a ratio of 0.5:1 [17,18].

N. Belov et al. report that there exist two possible invariant reactions for Si-rich Al-Si-Mg-Fe-Mn alloys (see reactions below) [17]. The reactions suggest that even though an Mn addition can transform the most detrimental phase, Al₅FeSi, into Al₁₅(Fe,Mn)₃Si₂, the AlFeMgSi phase will likely still be present. However, given that this phase forms in the presence of Mg, it is postulated that lowering the Mg content should minimize the amount of the phase to a reasonable level.



The deleterious effect that the harmful Fe-bearing intermetallics have on the mechanical properties of Al alloys has led to the following research. In the present study, the concentration of Mn and Mg in a RE-modified A356 alloy is adjusted to eliminate or minimize the amount of harmful β -Al₅FeSi and π -Al₉FeMg₃Si₅ precipitates. The effects that the chemistry modification has on the simulated evolution of phases, the microstructure, and the elevated temperature (250 °C) tensile and creep performance are investigated.

2. Experimental Procedure

This section outlines the experimental procedures used to evaluate the effects that various iron-bearing intermetallics have on the solidification characteristics, microstructure, and fitness-for-service performance of two RE-modified A356 alloys. Raw A356 ingots were melted in a gas-fired crucible furnace at Eck Industries' industrial manufacturing facility in Manitowoc, Wisconsin. To introduce the rare-earth elements, a 3.5 wt.% addition of light rare earth element mischmetal (~52 wt.% Ce, 26 wt.% La, 16 wt.% Nd, and 6 wt.% Pr) was added to the melt. The molten alloy was then mixed with an impeller speed of 250 RPM and then de-gassed and cleaned with argon for 20 min. The molten alloy was poured into an ASTM standard permanent tensile mold preheated to 400 °C. Focused on eliminating or minimizing the amount of the Al₉FeSi₃Mg₅ and Al₅FeSi phases in the A356RE samples, the Mn concentration was increased from 0.1 to 0.41 wt.%, while the Mg content was reduced from 0.49 to 0.25 wt.% (see Table 1 for alloy composition). To modify the concentration of elements in the A356RE-B alloy, an Al-25 wt.%Mn master alloy was introduced to the alloy melt.

Table 1. Average composition (wt.%) of modified A356RE alloys.

Alloy	Al	Mg	Si	Cu	Fe	Mn	Ti	Ce	La	Nd	Pr
A356RE-A ^a	Bal.	0.49	7.11	0.01	0.13	0.10	0.20	1.83	0.92	0.58	0.19
A356RE-B ^a	Bal.	0.25	6.15	0.01	0.13	0.41	0.20	1.83	0.92	0.58	0.19

^a—contains trace amounts of strontium and boron.

To verify that the casting process for both alloys was similar, the SDAS for each alloy was measured using an optical microscope. The average SDAS for over 50 Al grains for the A356RE-A and A356RE-B alloys were $39.1 \pm 6.5 \mu\text{m}$ and $36.4 \pm 7.5 \mu\text{m}$, respectively. The minimal change between both alloys confirms that the solidification cooling rates for

both samples were essentially equal. Such a small difference in the SDAS will likely have a negligible effect on the material's mechanical properties, especially when considering the standard deviations and, thus, the differences between the two alloys is presumed to be directly caused by the chemistry modification.

2.1. Thermodynamic Simulations (ThermoCalc™)

Commercially available thermodynamic simulation software, ThermoCalc™ (2021a, Thermo-Calc Software, Solna, Sweden), was used to determine the liquidus and solidus temperatures as well as the evolution of phases during equilibrium and non-equilibrium solidification (i.e., Scheil solidification). Utilizing the CALPHAD (CALculation of PHase Diagrams) method, ThermoCalc™ processes all available information (experimental and theoretical) on phase equilibria and thermochemical properties of an alloy system. A mathematical model containing adjustable variables is used to describe the thermodynamic properties of each of the phases. This is achieved by assessing the chemical and physical properties (i.e., Gibb's free energy, crystallography, type of bonding, order-disorder transitions, magnetic properties, etc.) of the system in the thermodynamic model. Due to the limitations of the TCAL7 ThermoCalc™ database, Nd and Pr could not be included in the solidification simulations.

2.2. Microstructure Analysis

Following the principles outlined in the ASTM standard E3-11 [20], each sample was mounted in fast-curing acrylic resin, sequentially ground with silicon-carbide paper (from 120 to 600 grit), and then polished with colloidal diamond suspension (from 9 μm to 1 μm). To further reveal the microstructure, each sample was electro-etched at 30 V in Barker's etchant (2.5 mL of fluoroboric acid in 200 mL of distilled water) for 15–20 s.

A field emission gun scanning electron microscope (Mira3 XMU, TESCAN, Brno-Kohoutovice, Czech Republic) operating at an accelerating voltage of 20 kV was used to characterize the microstructure. Oxford Instruments Aztec data acquisition and processing software (4.3, Oxford Instruments NanoAnalysis, High Wycombe, UK) with an 80 mm² Oxford EDS detector (Oxford Instruments, Abingdon, UK) were utilized for the composition analysis of the various phases. Morphology and EDS spectra for each phase were compared to the literature and the inorganic crystal structure database (ICSD) [21] to determine the approximate stoichiometry of each phase.

2.3. Fitness-for-Service Assessment

The elevated temperature tensile and creep tests for each alloy were performed using an MTS hydraulic material test system equipped with a 100 kN load frame, grips rated for 26 kN, a tri-chambered resistance furnace, three PID-controlled 0.04" k-type thermocouples, and a calibrated extensometer. Prior to commencing the FFS tests, each sample was conditioned for 200 h at 250 °C. Conditioning stabilizes the alloy's microstructure and provides more realistic data of how the alloys will perform in their design purpose (i.e., engine blocks, cylinder heads and turbochargers). After conditioning, each sample was placed in the test cell and heated at a rate of 0.5 °C/s until the desired temperature was reached. Once the controller reached the selected temperature, the system was held for 30 min or until the temperature of the sample and extension arms reached a steady-state and the thermally induced strain was no longer increasing. The temperature for each of the experiments was controlled using a PID controller with a precision of ± 0.5 °C.

Following the procedures outlined in the ASTM standards E8M [22], for high elevated temperature tensile testing, a strain rate of 0.005 mm/mm/min was applied until failure (equivalent to the sample breaking or a 90% reduction in the max force). The yield strength is reported as the 0.2% offset stress. The geometry of the sub-size tensile samples is shown below in Figure 1.

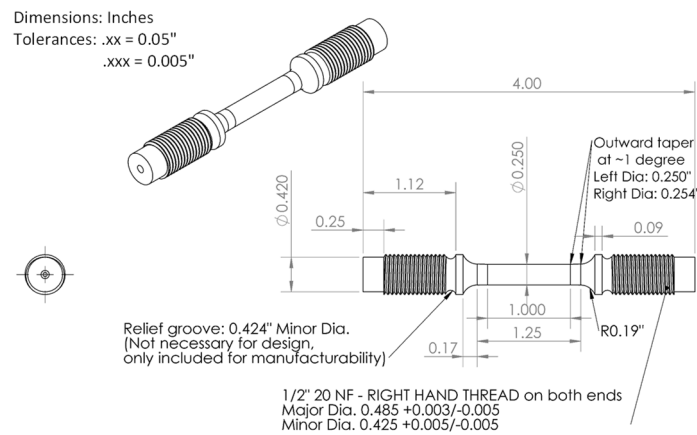


Figure 1. Geometry of tensile and creep samples (dimensions are in inches).

In addition to tensile strength, creep plays a large role in the premature failure of components that operate at elevated temperatures. Subjecting a material to a single constant stress for an extended period of time (i.e., until fracture or extensive elongation) provides an indication of how the alloy will perform for a particular application. The most useful information that is obtained from this type of test is the steady-state creep rate $\dot{\epsilon}_s$. The steady-state creep rate $\dot{\epsilon}_s$ is an important parameter that is often included in the design requirements for powertrain components. At moderate temperatures (0.4 to 0.5 T_{melt}), the steady-state creep rate is generally governed by a power-law (PL) relation and is calculated using Equation (1), where A is a material constant, σ is the applied stress, n_a is the apparent stress exponent, Q_a is the apparent activation energy for steady-state creep, R is the universal gas constant, and T is the absolute temperature [23,24]. The apparent stress exponent n_a and activation energy Q_a provide an indication of which creep mechanisms are predominant.

$$\dot{\epsilon}_s = A\sigma^{n_a} \exp\left(-\frac{Q_a}{RT}\right) \quad (1)$$

Q_a and n_a are calculated with Equations (2) and (3) and are obtained by performing creep tests at different temperatures and stresses. It should be noted that since only singular temperature creep tests were performed in the current study, the activation energy could not be calculated.

$$Q_a = -R \left[\ln\left(\frac{\dot{\epsilon}_1}{\dot{\epsilon}_2}\right) / \left(\frac{1}{T_1} - \frac{1}{T_2}\right) \right] \text{ at constant } \sigma \quad (2)$$

$$n_a = \left[\ln(\dot{\epsilon}_1 - \dot{\epsilon}_2) - \ln(\sigma_1 - \sigma_2) \right] \text{ at constant } T \quad (3)$$

Due to the complex interactions of dislocations with precipitates in multicomponent alloys containing a large number of intermetallics, inexplicably high apparent stress exponents ($n_a = 40$) and activation energies ($Q_a = 570 \text{ kJmol}^{-1}$) have been reported in the literature [25]. Such high values cannot be easily translated to realistic creep mechanisms. As a result, for dispersion-strengthened alloys, a threshold stress σ_{th} is introduced to account for the inexplicably high (with regard to the thermally activated dislocation mechanisms) and varying apparent n_a and Q_a values (see Equation (4), where G is the shear modulus). The threshold stress is estimated by plotting $\dot{\epsilon}_s^{1/n}$ vs. σ on a double-linear scale and extrapolating to $\dot{\epsilon}_s = 0$ for the region corresponding to apparent stress exponent values greater than $\sim 4.4\text{--}5$ [25]. When plotting $\dot{\epsilon}_s^{1/n}$ vs. σ , a stress exponent value of $n = 4.4$ to 5, or 7 can be used, which represents dislocation creep and lattice diffusion-controlled creep with a constant sub-grain structure, respectively [26–28]. The results can be verified by plotting the $\dot{\epsilon}_s$ vs. the effective stress ($\sigma - \sigma_{th}$) on a double-logarithmic scale and determining the goodness of fit (i.e., value of R^2).

$$\dot{\epsilon}_s = A \left(\frac{\sigma - \sigma_{th}}{G} \right)^n \exp\left(-\frac{Q}{RT}\right) \quad (4)$$

The presence of a threshold stress is not unanimously accepted within the scientific and materials engineering community, and the exact mechanisms are not completely understood. However, it has been postulated that for non-shearable precipitates, a threshold stress may develop due to the interaction of dislocations with precipitates during dislocation climb/bypass or the Orowan bowing mechanism [29]. Krug et al. [30] suggests that the elastic interactions of dislocations with precipitates facilitates the dislocation climb process; however, the dislocations are pinned on the departure side, which results in the development of a threshold stress. It is believed that dislocation creep is not significant below the threshold stress.

The basic steps of a staircase creep experiment include subjecting the sample to an applied stress (σ_1), holding for an extended period of time, releasing the stress for a short period of time, and then increasing the stress above σ_1 and holding. These steps are repeated until the material fails. The amount by which the applied stress is increased after each cycle is largely dependent on the material's mechanical properties. The stress increments in this study were held for ~20–24 h, and each of the “released” stresses (~2–3 MPa) were held for 1 hour.

A creep test consists of applying a constant stress to a creep sample (see Figure 1), while measuring the total plastic and elastic strain. The testing principles outline in ASTM E139-70 [31] should be followed. Typically, the magnitude of the applied stress corresponds to a stress value below the material's yield strength. Similar to a tensile test, the most common method of measuring the strain is via extensometers.

During operation, the critical components of the IC engines, such as cylinder block and engine head) heat up to 200–300 °C (depending on engine configuration and type of fuel) and as a result, the bulk of the material attempts to expand. However, its natural expansion is restricted by the surrounding material and the preload from fasteners. This restriction has been reported to result in the development of stress on the magnitude of 22–30 MPa [32]. These values can be further increased to 45–50 MPa when coupled with the cylinder power stroke pressures of up to 20 MPa [33]. As a result, the creep experiments conducted in this study begin at 22 MPa and progressively increase until the sample fails. Due to the complex nature of creep in multicomponent alloys (i.e., powertrain alloys), the rates controlling creep mechanisms are commonly described with reference to the deformation mechanism map (see Figure 2) of the element of highest concentration, (i.e., aluminum for Al-based alloys or magnesium for Mg-based alloys) [34–36]. The vertical dashed line shown in Figure 2 represents the homologous temperature (T_m/T) for the test temperature of 250 °C.

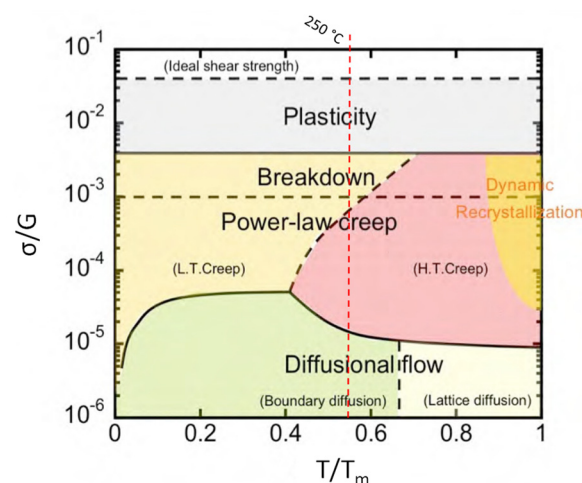


Figure 2. Deformation mechanism map for pure Al, original [34], adapted from [35].

Depending on the material's temperature-dependent shear modulus, G , and the applied stress, σ , the steady-state creep rate may be described by any of the creep mechanisms shown in Figure 2. For Al powertrain alloys tested between $\sim 150\text{--}300\text{ }^\circ\text{C}$, the rate-controlling creep mechanisms are diffusional creep (low stresses), high temperature creep and power-law-governed dislocation climb (moderate stress), power-law-breakdown dislocation creep (moderate to high stress) and, eventually, dislocation glide and plasticity (high stress).

3. Results and Discussion

3.1. Thermodynamic Simulations

The equilibrium solidification diagram for the A356RE-A alloy is shown below in Figure 3. The simulation suggests that, at room temperature, the alloy should consist of Al, eutectic Si, $\text{Al}_4\text{Ce}_3\text{Si}_6$, $\text{Al}_{11}\text{La}_3$, $\text{Al}_5\text{Cu}_2\text{Mg}_8\text{Si}_6$, $\text{Al}_9\text{Fe}_2\text{Si}_2$, $\text{Al}_3\text{Ti}_{\text{LT}}$, Mg_2Si , and $\text{Al}_{15}(\text{Fe},\text{Mn})_3\text{Si}_2$. The mass fraction of each phase is listed in Table 2. In addition to these phases, some metastable phases were also observed to form during the solidification process, specifically AlCeSi , AlCeSi_2 , $\text{LaSi}_2\text{-A1}$, $\text{LaSi}_2\text{-A2}$, and AlSi_3Ti_2 .

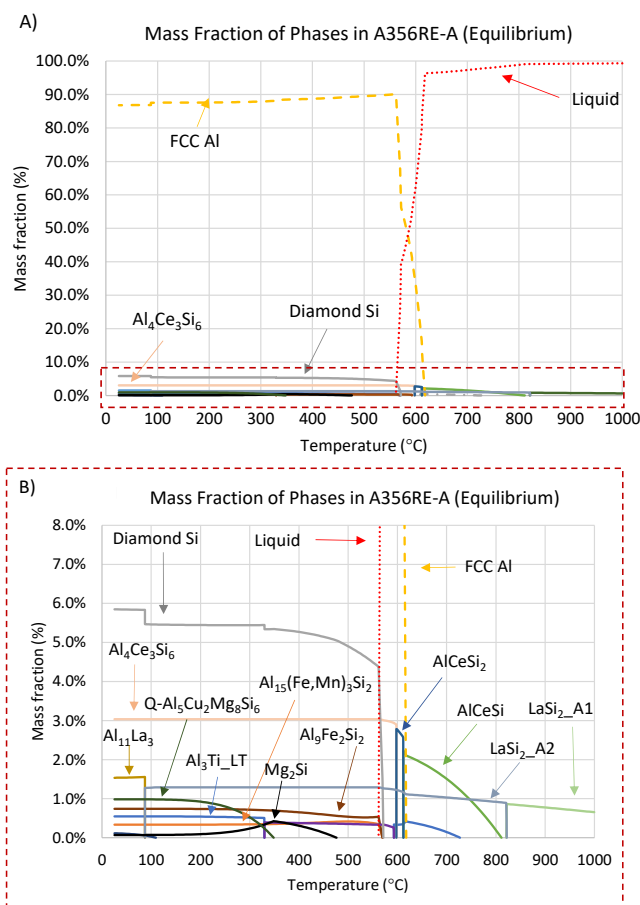


Figure 3. Mass fraction of phases in A356RE-A alloy (A) full solidification process, (B) progression of minority phase solidification (equilibrium solidification).

Due to the high melting temperature of the La-Si phases, a small mass fraction of the $\text{LaSi}_2\text{-A1}$ phase was observed above $1000\text{ }^\circ\text{C}$ (i.e., $\sim 0.6\%$) which transforms into $\text{LaSi}_2\text{-A2}$ at $822\text{ }^\circ\text{C}$. Subsequently, the nucleation of the AlCeSi phase begins at $811\text{ }^\circ\text{C}$. This phase reaches a maximum mass fraction of 2.23% at $612\text{ }^\circ\text{C}$ before temporarily transforming into AlCeSi_2 and then, finally, into $\text{Al}_4\text{Ce}_3\text{Si}_6$ which reaches a maximum mass fraction of 3.03% . The $\text{Al}_4\text{Ce}_3\text{Si}_6$ phase has been reported to improve the thermal stability of Al-Si-RE alloys [1] and is one of the reasons for the impressive increase in elevated temperature

strength of the A356 system [14]. In addition to the $\text{Al}_4\text{Ce}_3\text{Si}_6$ phase, the presence of La in the RE mischmetal led to the formation of $\text{Al}_{11}\text{La}_3$. This phase has nearly identical properties as the $\text{Al}_{11}\text{Ce}_3$ phase, and its presence further improves the alloy's thermal stability [37].

Combating the positive benefits from the thermally stable $\text{Al}_{11}\text{La}_3$ and $\text{Al}_4\text{Ce}_3\text{Si}_6$ phases, $\sim 0.74\%$ of the harmful $\text{Al}_9\text{Fe}_2\text{Si}_2$ phase was observed. The $\text{Al}_9\text{Fe}_2\text{Si}_2$ phase is also commonly reported as Al_5FeSi . The nucleation of this phase begins at $\sim 570^\circ\text{C}$, which is followed by a rapid increase in the mass fraction to 0.53%. Subsequently, the mass fraction of this phase slowly increases until about 140°C , after which the mass fraction remains relatively unchanged. Congruently, the more desirable $\text{Al}_{15}(\text{Fe},\text{Mn})_3\text{Si}_2$ phase begins to nucleate just prior to the onset of the $\text{Al}_9\text{Fe}_2\text{Si}_2$ phase, reaching a maximum mass fraction of 0.43%. This suggests that due to the low amount of Mn in the alloy (i.e., 0.1 wt.%), the $\text{Al}_9\text{Fe}_2\text{Si}_2$ phase is the preferential Fe phase to form. This supports the work done by N. Below et al. [17].

The nucleation and solidus temperature of FCC-Al was observed to be 617 and 562°C , respectively. The moderate solidification range (i.e., 55°C) of FCC-Al suggests that porosity, caused by slow solidification, should not be a considerable issue.

Due to moderate Mg concentration in the A356RE-A alloy, it was expected that the $\text{Al}_9\text{FeMg}_3\text{Si}_5$ would be observed in the solidification diagram but, instead, part of the Mg forms a solid solution with the Al matrix and the rest is present in the $\text{Q_Al}_5\text{Cu}_2\text{Mg}_8\text{Si}_6$ phase. Fortunately, the $\text{Q_Al}_5\text{Cu}_2\text{Mg}_8\text{Si}_6$ phase improves the thermal stability of the alloy and is much more desirable as compared to the $\text{Al}_9\text{FeMg}_3\text{Si}_5$ phase.

Table 2. Mass fraction of phases in A356RE-A.

Phases	Mass Fraction (%)	
	Equilibrium (25°C)	Scheil (532°C)
FCC Al	BAL.	BAL.
Diamond (Si)	5.85	4.69
$\text{Al}_4\text{Ce}_3\text{Si}_6$	3.03	0.15
AlCeSi_2	0 (2.79) *	0.25
AlCeSi	0 (2.23) *	2.22
$\text{Al}_{11}\text{La}_3$	1.56	-
$\text{LaSi}_2\text{-A2}$	0 (1.29) *	0.40
$\text{Q_Al}_5\text{Cu}_2\text{Mg}_8\text{Si}_6$	0.98	-
$\text{LaSi}_2\text{-A1}$	0 (0.86) *	0.86
$\text{Al}_9\text{Fe}_2\text{Si}_2$	0.74	0.43
$\text{Al}_3\text{Ti_LT}$	0.55	0.41
Mg_2Si	0.43	0.16
$\text{Al}_{15}(\text{Fe},\text{Mn})_3\text{Si}_2$	0.42	0.37
AlSi_3Ti_2	0 (0.39) *	-
$\text{Al}_{18}\text{Fe}_2\text{Mg}_7\text{Si}_{10}$	-	0.26

Note: (max values). *—Metastable at specific temperature (see Figure 3).

The Scheil diagram for the A356RE alloy is shown below in Figure 4. Due to the assumptions associated with Scheil solidification, the AlCeSi phase could not transform in the AlCeSi_2 or $\text{Al}_4\text{Ce}_3\text{Si}_6$ phases. Similarly, the growth of the $\text{Q_Al}_5\text{Cu}_2\text{Mg}_8\text{Si}_6$ phase was also halted by the assumption that zero diffusion occurs in the solid state. The non-equilibrium mode of solidification appears to have resulted in the formation of the $\text{Al}_9\text{FeMg}_3\text{Si}_5$ phase (i.e., $\text{Al}_{18}\text{Fe}_2\text{Mg}_6\text{Si}_{10}$ phase). The presence of this phase suggests that, depending on the cooling rate, this phase may or may not be present in the microstructures. However, it is likely that a combination of equilibrium and non-equilibrium solidification will occur, and thus, it is expected that some of this phase will be present at room temperature. The Scheil diagram indicates that this phase begins to nucleate at 556°C and reaches a maximum mass fraction of 0.26% by 532°C . In addition to this phase, the $\text{Al}_9\text{Fe}_2\text{Si}_2$ phase was also observed, however in a considerably lower amount ($\sim 0.43\%$).

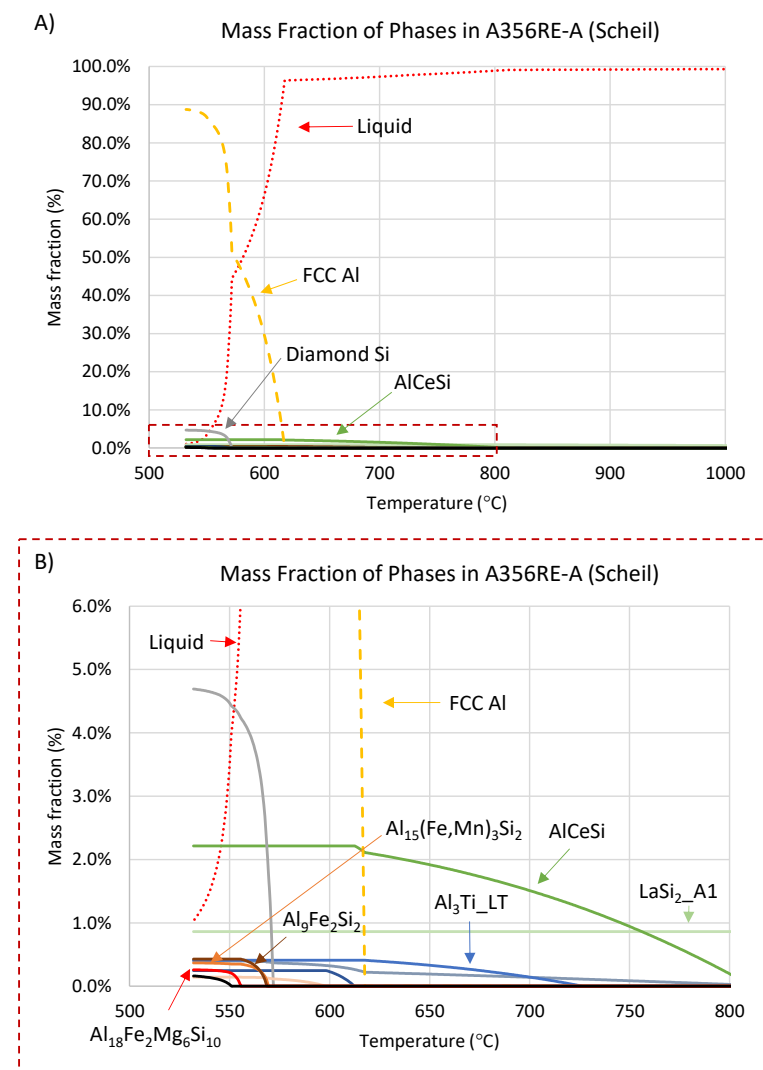


Figure 4. Mass fraction of phases in A356RE-A (A) full solidification process, (B) progression of minority phase solidification (non-equilibrium solidification).

The equilibrium solidification diagram for A356RE-B (high Mn, low Mg alloy) is shown below in Figure 5. The results from the equilibrium simulation suggest that the chemistry modification greatly increases the volume fraction of the $\text{Al}_{15}(\text{Fe},\text{Mn})_3\text{Si}_2$ phase (i.e., from 0.42 to 1.75%) while reducing the mass fraction of the $\text{Al}_9\text{Fe}_2\text{Si}_2$ by ~65% (i.e., from 0.74% to 0.48%). The chemistry modification had a negligible effect on the mass fraction or solidification kinetics of the RE-containing phases (see Table 3). Moreover, it was observed that nucleation and solidus temperature of FCC-Al increased by only ~5 °C.

Interestingly, the chemistry modification greatly reduced the amount of the $\text{Q_Al}_5\text{Cu}_2\text{Mg}_8\text{Si}_6$ phase (i.e., 0.15 vs. 0.98%) and it was observed that this phase reaches a mass fraction of 0% by just ~240 °C as compared to 340 °C in A356RE-A. The reduction in mass fraction is likely caused by the lower amount of available Mg. The reduction in Mg did not significantly affect the maximum mass fraction of Mg_2Si (i.e., 0.37% vs. 0.43%) but it did slightly alter the solidification kinetics. In A356RE-A, it was observed that at room temperature, the mass fraction of Mg_2Si was just 0.069%; however, for A356RE-B the mass fraction was 0.32%. It appears that the $\text{Al}_5\text{Cu}_2\text{Mg}_8\text{Si}_6$ forms at the expense of Mg_2Si , and thus the lower volume fraction of $\text{Al}_5\text{Cu}_2\text{Mg}_8\text{Si}_6$ in A356RE-B results in the greater volume fraction of Mg_2Si . Fortunately, the mass fraction of Mg_2Si is nearly at its maximum at 250 °C, suggesting that its hardening contribution will also be at its greatest.

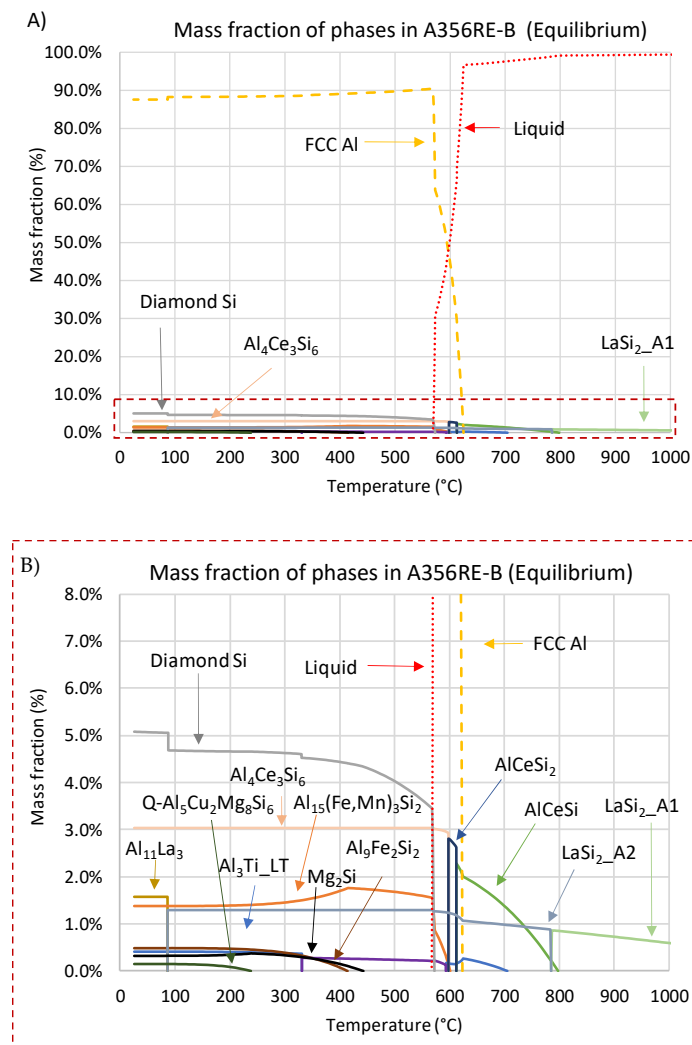


Figure 5. Mass fraction of phases in the A356RE-B alloy (A) full solidification process, (B) progression of minority phase solidification (equilibrium solidification).

Table 3. Mass fraction of phases in A356RE-B.

Phases	Mass Fraction (%)	
	Equilibrium (25 °C)	Scheil (554 °C)
FCC Al	BAL.	BAL.
Diamond (Si)	5.08	3.92
Al ₄ Ce ₃ Si ₆	3.03	0.12
AlCeSi ₂	0 (2.81) *	0.20
AlCeSi	0 (2.29) *	2.28
Al ₁₁ La ₃	1.58	-
LaSi ₂ _A2	0 (1.29) *	0.41
Q-Al ₅ Cu ₂ Mg ₈ Si ₆	0.15	-
LaSi ₂ _A1	0 (0.85) *	0.85
Al ₉ Fe ₂ Si ₂	0.48	0.08
Al ₃ Ti_LT	0.41	0.26
Mg ₂ Si	0.37	0.07
Al ₁₅ (Fe,Mn) ₃ Si ₂	1.75	1.23
AlSi ₃ Ti ₂	0 (0.28) *	-
Al ₁₈ Fe ₂ Mg ₇ Si ₁₀	-	0.20

Note: (max values). *—Metastable at a specific temperature (see Figure 5).

The Scheil simulation of A356RE-B reveals similar observations as described for the equilibrium simulation (see Figure 6). The mass fraction of the $\text{Al}_9\text{Fe}_2\text{Si}_2$ was further decreased, reaching only 0.08%. Similar levels of the $\text{Al}_{15}(\text{Fe,Mn})_3\text{Si}_2$ phase were also observed, reaching a maximum of 1.32%. However, a small mass fraction of the undesirable $\text{Al}_9\text{FeMg}_3\text{Si}_5$ phase was also present at the end of the Scheil simulation. Similar to the discussion for A356RE-A, it is expected that a combination of both equilibrium and non-equilibrium solidification will occur during the actual casting process.

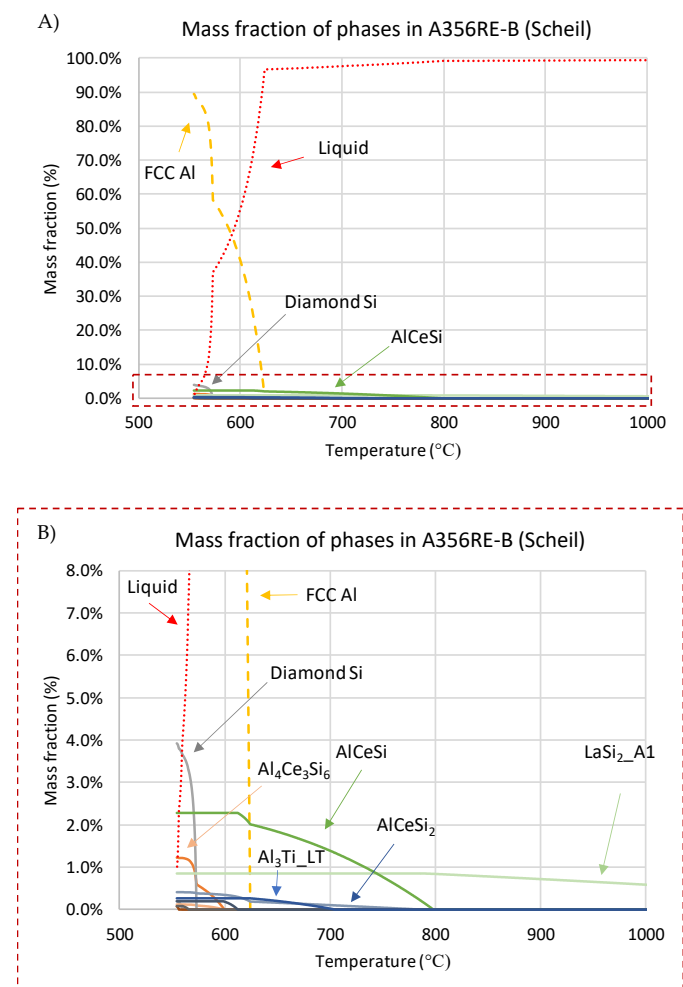


Figure 6. Mass fraction of phases in the A356RE-B alloy (A) full solidification process, (B) progression of minority phase solidification (non-equilibrium solidification).

The thermodynamic simulations of A356RE-B suggest that the modified Mn and Mg concentration should result in a lower concentration of harmful Fe-bearing intermetallics, while having little negative effect on the RE-bearing intermetallics or solidification characteristics of the alloy. As a result, it is expected that A356RE-B will be superior during the fitness-for-service testing.

3.2. Microstructure

Optical and SEM micrographs of the A356RE-A alloy are shown below in Figures 7 and 8. The microstructure of the alloy primarily consists of primary Al dendrites, flaky Si particles, a plate-like AlSiRE intermetallic and needle-like Fe-containing phases. The morphology and composition (see Table 4) of the Fe-containing phases suggests that they are Al_5FeSi and $\text{Al}_9\text{FeMg}_3\text{Si}_5$, which correlates well with the ThermoCalc results (see Figures 2 and 3). The difference in the Si and Fe concentration for the Al_5FeSi shown in Table 4 is likely attributed to the high penetration of the electron beam, which is on the same magnitude

as the near nano-size needle-like precipitates. As a result, the composition of this phase is slightly skewed due to the underlying Al matrix and Si particles. The combined area fraction of these two Fe phases reached $2.9 \pm 0.85\%$.

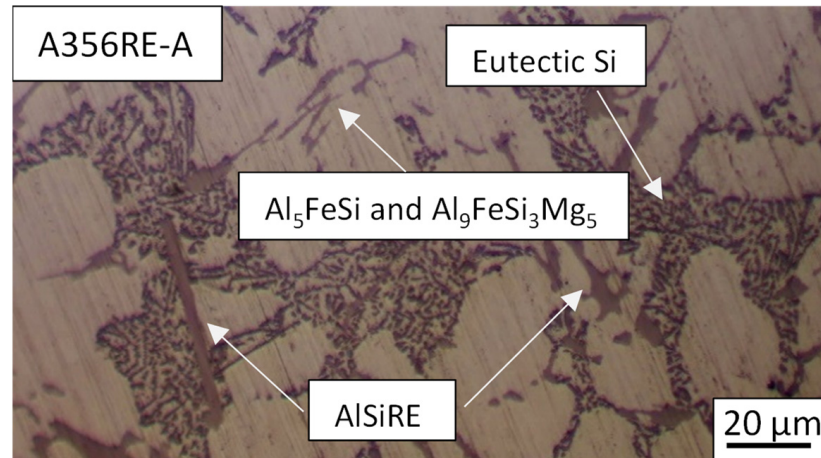


Figure 7. Optical micrograph of A356RE-A.

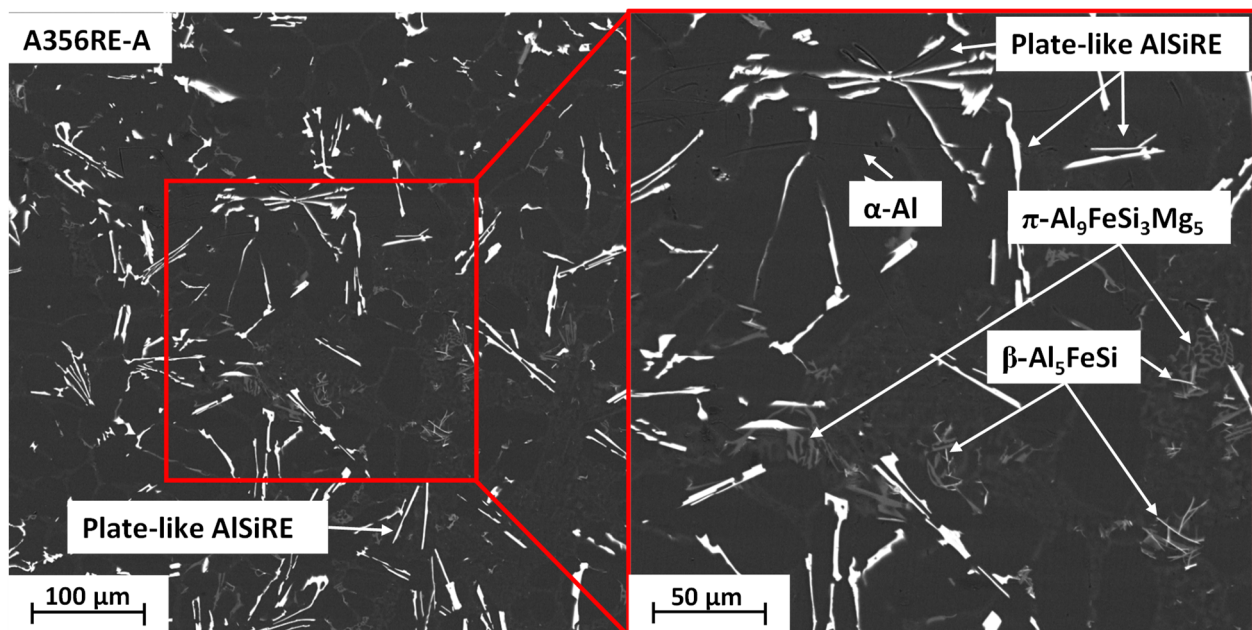


Figure 8. SEM micrograph of A356RE-A (left) 500 \times , (right) 1000 \times .

Table 4. Composition of phases in A356RE-A (at.%).

Phase	Al	Si	Fe	Mg	Ce	La	Nd	Ti	Ni	Mn
Al	Bal	1.37 ± 0.01	-	-	-	-	-	0.14 ± 0.01	-	-
AlSiRE	Bal	37.84 ± 0.96	-	-	16.03 ± 3.08	7.12 ± 2.03	6.68 ± 1.36	-	-	-
Al ₂₀ Ti ₂ RE	Bal	2.13 ± 0.89	-	-	3.79 ± 0.20	-	0.48 ± 0.03	7.69 ± 0.20	-	-
Al ₉ FeSi ₃ Mg ₅	Bal	23.32 ± 3.25	2.97 ± 0.19	9.92 ± 0.58	0.22 ± 0.04	-	0.09 ± 0.01	-	0.15 ± 0.04	0.38 ± 0.04
Al ₅ FeSi	Bal	9.88 ± 3.25	2.23 ± 0.85	0.74 ± 0.23	0.09 ± 0.03	-	-	-	0.19 ± 0.05	0.54 ± 0.21

The morphology of the Al₉FeMg₃Si₅ phase is blocky and interconnected, and this phase is present in a larger volume fraction as compared to the more harmful needle-like Al₅FeSi phase. The Al₁₁La₃ and Q_{Al₅Cu₂Mg₈Si₆} phases shown in the simulated

solidification charts (see Figures 3 and 4) were not observed in the microstructure. This is believed to be attributed to the high concentration of La and Mg in the AlSiRE and $\text{Al}_9\text{FeSi}_3\text{Mg}_5$ phases, respectively. The measured area fraction of the AlSiRE phase was determined to be $4.85 \pm 1.23\%$.

An optical micrograph of the modified A356RE alloy (i.e. A356RE-B) is shown below in Figure 9. The Mn addition appears to have reduced the interparticle spacing of eutectic Si particles while also decreasing the size of the eutectic colonies (compare Figures 7 and 9). These changes are expected to improve the alloy's fitness-for-service performance via the Crowan mechanism [38].

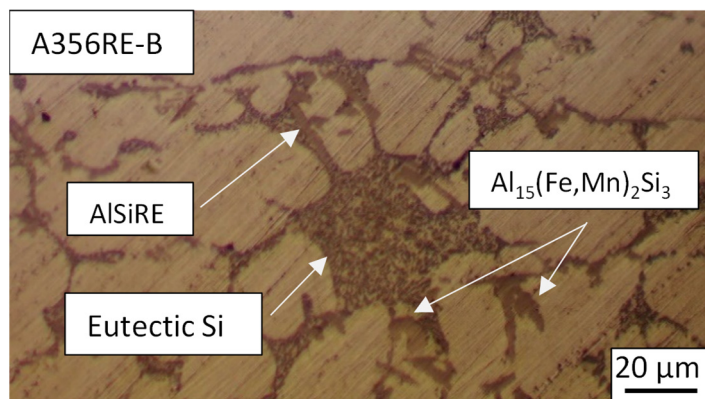


Figure 9. Optical micrograph of A356RE-B (low Mg, high Mn).

The SEM micrograph below (see Figure 10) shows that the modified composition did, indeed, result in the partial transformation of the harmful Fe-containing phases into $\text{Al}_{15}(\text{Fe,Mn})_3\text{Si}_2$ (area fraction = $3.54 \pm 0.93\%$). Not all of the harmful Al_5FeSi and $\text{Al}_9\text{FeSi}_3\text{Mg}_5$ precipitates were transformed; however, their combined area fraction reached only $0.55 \pm 0.25\%$ as compared to the 2.9% observed in A356RE-A. The volume fraction of the AlSiRE phase remained essentially unchanged, reaching 4.85 ± 1.36 . The combined contribution of the temperature-resistant AlSiRE phase and the tough $\text{Al}_{15}(\text{Fe,Mn})_3\text{Si}_2$ phase is expected to improve the fitness-for-service performance of the alloy.

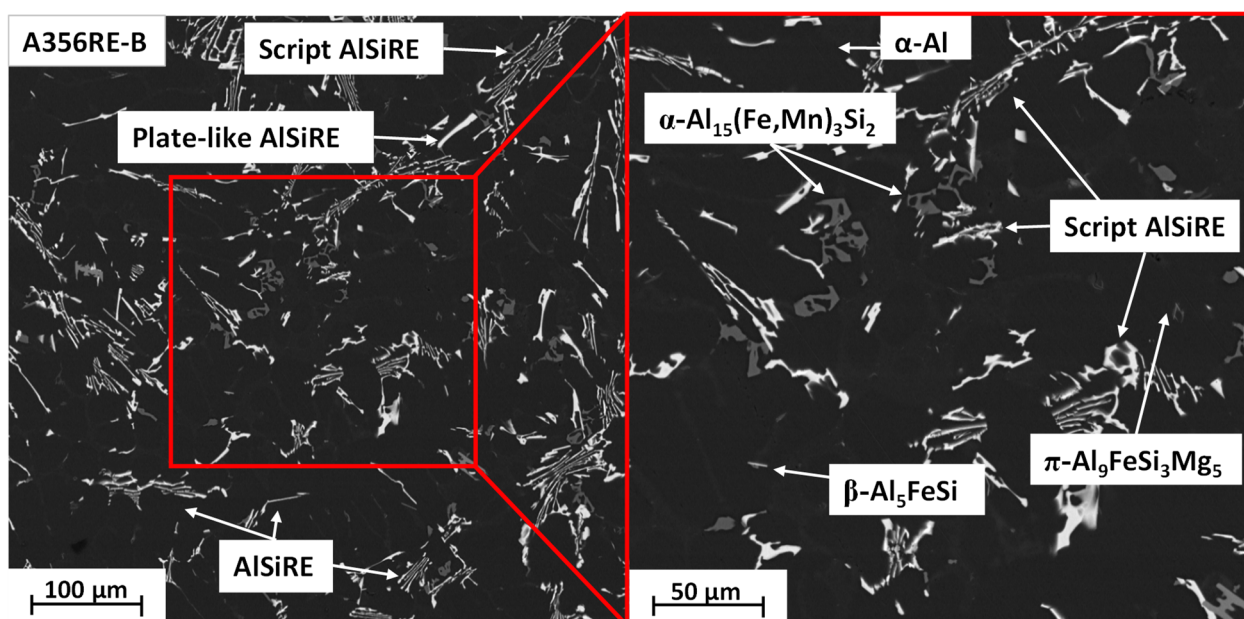


Figure 10. SEM micrograph of A356RE-B (left) 500 \times , (right) 1000 \times (low Mg, high Mn).

The concentration of RE elements in the AlSiRE phase seems to have increased slightly in A356RE-B as compared to A356RE-A (see Tables 4 and 5). In addition, it was observed that the morphology of the AlSiRE phase appears to have shifted from the elongated rod/plate-like structure in A356RE-A toward a smaller and more interconnected Chinese script shape. In the A356RE-A alloy, the AlSiRE phase was observed to form predominantly with the plate-like morphology (~90–95%), whereas the plate-like morphology was present in less than 5% in the A356RE-B alloy. The faceted growth of the AlSiRE phase in A356RE-B suggests that this alloy may have improved resistance against dislocation motion as compared to A356RE-A. Combined with the higher area fraction of the tougher and less stress-concentrating $\text{Al}_{15}(\text{Fe},\text{Mn})_3\text{Si}_2$ phase, it is expected that A356RE-B will perform superiorly during the elevated-temperature tensile and creep tests.

Table 5. Composition of phases in A356RE-B (at.% \pm standard deviation).

Phase	Al	Si	Fe	Mg	Ce	La	Nd	Ti	Ni	Mn
Al	Bal.	1.15 \pm 0.06	-	-	-	-	-	-	-	0.10 \pm 0.05
AlSiRE	Bal.	35.21 \pm 0.23	-	0.73 \pm 0.70	11.65 \pm 3.40	4.43 \pm 0.08	4.24 \pm 1.88	-	-	-
$\text{Al}_{20}\text{Ti}_2\text{RE}$	Bal.	-	-	-	4.79 \pm 0.58	0.35 \pm 0.1	0.99 \pm 0.99	6.66 \pm 0.15	-	-
$\text{Al}_9\text{FeSi}_3\text{Mg}_5$	Bal.	26.74 \pm 1.25	3.04 \pm 0.47	19.86 \pm 0.44	-	-	-	-	2.98 \pm 0.56	1.84 \pm 0.03
Al_5FeSi	Bal.	8.85 \pm 3.12	2.25 \pm 0.69	0.68 \pm 0.28	0.04 \pm 0.01	-	-	-	0.25 \pm 0.05	0.37 \pm 0.22
$\text{Al}_{15}(\text{Fe},\text{Mn})_3\text{Si}_2$	Bal.	12.67 \pm 0.26	4.21 \pm 0.12	-	-	-	-	-	-	11.90 \pm 0.15

3.3. Fitness-for-Service

To determine how the microstructural differences between A356RE-A and A356RE-B affect the fitness-for-service performance of the alloy system, elevated temperature tensile and creep tests were performed on the two alloys. The tensile results of both alloys at 250 °C are shown below in Figure 11. The YS and UTS of the A356RE-A alloy were determined to be 62 and 84.3 MPa, respectively. As compared to the tensile results for the original as-cast A356 + 3.5%RE alloy reported in [14], the new cleaning process (i.e., mechanical mixing + argon-purging) has notably increased both the YS (from 56 to 62 MPa) and UTS (from 70 to 84 MPa). In addition, the modulus of elasticity increased from 56.3 to 64.2 GPa, respectively. Powertrain components that operate at elevated temperatures require sufficient stiffness to maintain tight dimensional tolerances; however, these applications also benefit from some degree of ductility which provides automotive manufacturers with another type of safety factor (i.e., the component will deform before cracking).

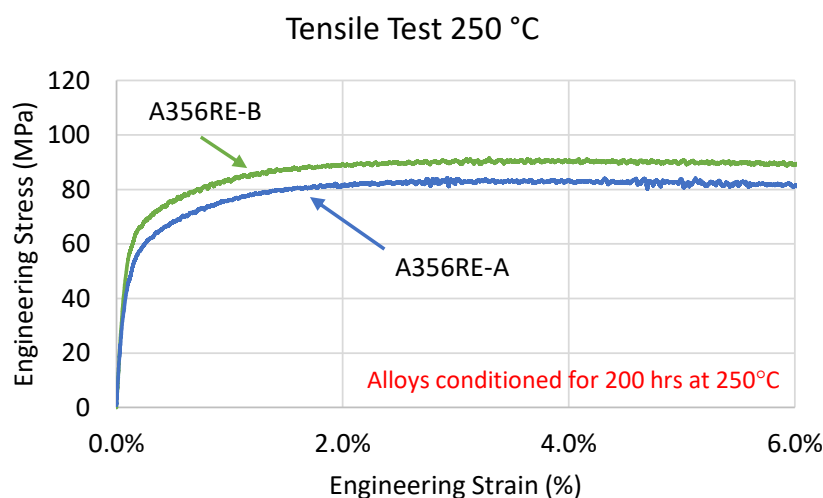


Figure 11. Tensile test results at 250 °C (conditioned for 200 h at test temperature).

As compared to the A356RE-A alloy, the modified A356RE-B alloy performed markedly better. Specifically, the YS, UTS, and modulus of elasticity improved by ~14%, 9%, and 10%, respectively. Moreover, the elongation also increased from 8.9 to 9.6%. As compared to the original A356RE alloy [14], the YS (i.e., 70.5 MPa), UTS (i.e., 91.5 MPa) and modulus of elasticity (i.e., 70.9 GPa) improved by ~25%, 31%, and 26%, respectively. The improved tensile performance of A356RE-B is believed to be attributed to three events, the first being the transformation of the harmful needle-like Fe phase to the more favourable $\text{Al}_{15}(\text{Fe},\text{Mn})_2\text{Si}_3$. This phase transformation leads to lower stress concentrations and interfacial energy while increasing the contribution from Orowan strengthening. Similarly, the partial transformation of the AlSiRE phase from elongated plates to smaller, faceted Chinese script improves the strength via the Hall-Petch relationship (i.e., the smaller the precipitate, the greater the resistance against dislocation motion). The last contribution to improved strength is related to the noticeable decrease in the interparticle spacing of the eutectic Si particles (compare Figures 7 and 9).

The staircase creep results for A356RE-A are shown below in Figure 12, and the steady-state creep rates for each stress are listed in Table 1. At 22 MPa, the $\dot{\epsilon}_s$ was measured to be $9.02 \times 10^{-10} \text{ s}^{-1}$. Such a slow $\dot{\epsilon}_s$ suggests that diffusion-based creep is the rate-controlling mechanism. It should be noted, however, that to accurately measure such low creep rates, a much longer time interval is required (on the order of several days to weeks). One of the reasons for this is due to the limited precision of extensometers as well as the natural force and thermal fluctuations that occur during creep tests.

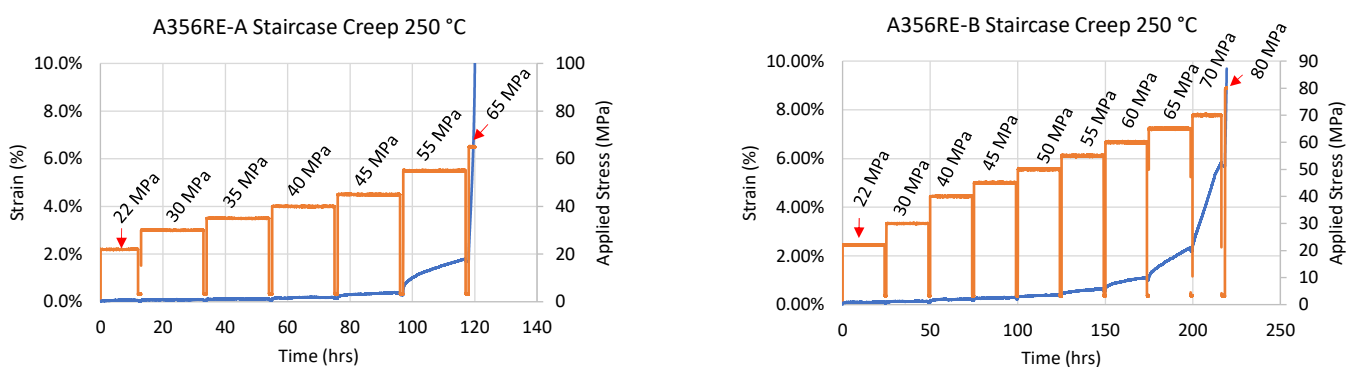


Figure 12. Staircase creep results at 250 °C (conditioned for 200 h at 250 °C).

Increasing the applied stress from 22 to 30 and finally 35 MPa resulted in only a small increase in the $\dot{\epsilon}_s$, reaching a maximum of $2.66 \times 10^{-9} \text{ s}^{-1}$. The calculated apparent stress exponent from 22 to 35 MPa was $n_a = 2.4$ (see Figure 13). This suggests that the diffusional creep at 22 MPa is transitioning to viscous drag and climb [39,40]. Increasing the stress to 40, 45, and finally 55 MPa quadruples the apparent stress exponent to $n_a = 10.0$, indicating that creep deformation bypassed power-law-governed dislocation climb, and transitioned to power-law breakdown dislocation creep. Such a high apparent stress exponent suggests that a threshold stress is present, likely present due to the high volume fraction of hard intermetallics in the alloy which pins dislocations [30]. Plotting $\dot{\epsilon}_s^{1/n}$ vs. σ , with $n = 4.4, 5$ and 7 revealed that $n = 7$ results in the greatest linear fit ($R^2 = 0.998$), suggesting that deformation is governed by lattice diffusion-controlled creep with a constant sub grain structure. Following the procedure described in [41], the threshold stress was determined to be ~34.3 MPa (see red arrows in Figure 13). The following increase in the applied stress (i.e., to 65 MPa) caused rapid elongation; the sample failed in ~2 h. A true steady-state creep was not established; however, the brief minimum creep rate was determined to be $7.99 \times 10^{-6} \text{ s}^{-1}$. Such a large increase in the creep rate caused a near-instantaneous transition through dislocation glide into plasticity ($n_a = 38.9$) [42].

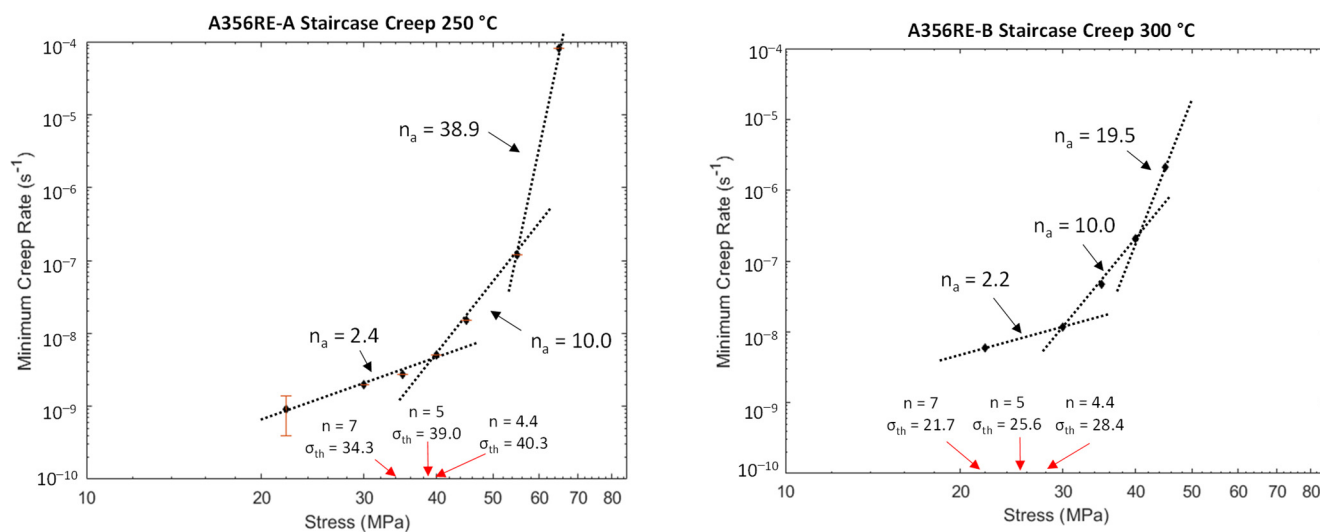


Figure 13. Minimum creep rate as a function of applied stress for A356RE-A at 250 °C. Note apparent stress exponent n_a and threshold stress σ_{th} .

The effects from the chemistry modification (increased Mn, decreased Mg) are clear from the clear increase in the material's creep resistance (see Figures 12 and 13). Specifically, at every stress, the $\dot{\epsilon}_s$ was lower for A356RE-B than for A356RE-A (see Table 6). Moreover, A356RE-B failed at a stress $\sim 10\text{--}15$ MPa greater than A356RE-A, reaching 100% of A356RE-B's measured YS. At 65 MPa (i.e., the fracture stress of A356RE-A), the $\dot{\epsilon}_s$ for A356RE-B was more than a full magnitude lower than observed for A356RE-A, reaching just $1.12 \times 10^{-7} \text{ s}^{-1}$ as compared to $7.99 \times 10^{-6} \text{ s}^{-1}$. In fact, the creep rate for the A356RE-B was a well-established steady-state creep rate, as opposed to the brief minimum creep rate for A356RE-A.

Table 6. Steady-state creep rates for A356RE-A and A356RE-B at 250 °C (units: $10^{-8}/\text{s}$).

Alloy	22 (MPa)	30 (MPa)	35 (MPa)	40 (MPa)	45 (MPa)	50 (MPa)	55 (MPa)	60 (MPa)	65 (MPa)	70 (MPa)	80 (MPa)
A356RE-A	0.09	0.20	0.27	0.50	1.53	-	12.10	-	798.58 *	-	-
A356RE-B	0.07	0.10	-	0.28	0.47	0.87	1.87	3.32	11.74	62.19	965.81 *

*—sample failed.

The steady-state creep rate at 22 MPa was determined to be $6.57 \times 10^{-10} \text{ s}^{-1}$. Similar to the discussion for A356RE-A, accurate measurement of such a low strain rate is difficult without subjecting the stress for several days to weeks. Thus, there is expected to be some minor error associated with the measurement at 22 MPa. Once the stress on the A356RE-B alloy was increased from 22 to 30 MPa, the resulting creep rate was half that of A356RE-A (i.e., $1.03 \times 10^{-9} \text{ s}^{-1}$ vs. $2.00 \times 10^{-9} \text{ s}^{-1}$, respectively). The calculated apparent stress exponent was also lower, reaching only $n_a = 1.1$ (as compared to $n_a = 2.4$). Such a low n_a suggests that diffusional creep is the rate-controlling mechanism. Further increasing the stress to 40 and 45 MPa only slightly raised the creep rate, reaching a maximum of $4.7 \times 10^{-9} \text{ s}^{-1}$. Albeit only a small increase, the calculated apparent stress exponent increased to $n_a = 4.2$, suggesting that the dominant creep mechanism has transitioned from diffusion creep to power-law-governed dislocation climb [39,40]. This correlates well with the deformation mechanism map (see Figure 2). Increasing the applied stress from 55 to 65 MPa raises the $\dot{\epsilon}_s$ by a magnitude, reaching $3.32 \times 10^{-8} \text{ s}^{-1}$. As a result, the power-law breaks down and dislocation creep is the now rate-controlling mechanism ($n_a = 11.0$) [42]. This is dissimilar from the deformation mechanism map for pure Al (see Figure 2). According to the deformation map and the calculated shear modulus (26.6 GPa), the power-law should breakdown with an applied stress of ~ 133 MPa. This

difference is likely attributed to the high-volume fraction of precipitates in A356RE-B as compared to pure Al. Further increasing the stress to 70 MPa leads to a complete breakdown of the power-law, and as a result, the dislocation creep transitions to dislocation glide ($n_a = 21.2$) [42]. It should be noted that the $\dot{\epsilon}_s$ at 70 MPa was more than a full magnitude lower for A356RE-B than at 65 MPa for A356RE-A. Finally, once the stress is increased to 80 MPa, the creep enters the plasticity regime where the sample begins to neck and, ultimately, leads to failure.

Similar to the A356RE-A alloy, the high apparent stress exponents suggest that there is a threshold stress in the A356RE-B alloy. Plotting $\dot{\epsilon}_s^{1/n}$ vs. σ reveals good linear fits for all three stress exponents, with $n = 7$ having the greatest fit at $R^2 = 0.983$, leading to an estimated threshold stress of 44.2 MPa.

The chemistry modification has clearly led to an increase in the creep resistance of the alloy. Not only has the threshold stress increased by ~ 10 MPa, the steady-state creep rates are lower at every stress. This is likely attributed to the higher volume fraction of intermetallics available for pinning dislocations, the transformation of the brittle Al_5FeSi and $\text{Al}_9\text{FeMg}_3\text{Si}_5$ into $\text{Al}_{15}(\text{Fe,Mn})_3\text{Si}_2$, as well as the size reduction and morphology modification of the AlSiRE intermetallic.

Similar to the results presented by A. Farkoosh and M. Pekguleryuz [33] who studied the effects of Mn on the creep resistance of Al-Si-Cu-Mg-Ni alloys, the increased Mn addition in the A356RE alloy not only lowered the steady-state creep rates for all stresses but also raised the fracture stress. The driving factors behind the observed improved strength and creep resistance is believed to be the transformation of Al_5FeSi and $\text{Al}_9\text{FeSi}_3\text{Mg}_5$ into $\text{Al}_{15}(\text{Fe,Mn})_3\text{Si}_2$ phase, as well as the partial transformation of the elongated AlSiRE plates into a smaller, faceted Chinese script morphology. The lower aspect ratio, a stronger bonding with the Al matrix, and the more favorable morphology of $\text{Al}_{15}(\text{Fe,Mn})_3\text{Si}_2$ phase lead to a decrease in the precipitate-matrix interfacial energy, lower the development of stress concentrations and improve the alloy's ductility. Moreover, this transformation increased the total volume fraction of intermetallics, leading to a greater number of obstacles available to pin dislocation motion (Orowan strengthening), and thereby, further improving the creep resistance of the alloy.

4. Conclusions

The study aimed to determine the effects that modifying the Mn and Mg concentrations in an A356 + 3.5 wt.% RE mischmetal alloy has on microstructure, and elevated temperature tensile and creep performance. Focused on transforming the harmful Al_5FeSi and $\text{Al}_9\text{FeSi}_3\text{Mg}_5$ iron phases into the more favorable $\text{Al}_{15}(\text{Fe,Mn})_3\text{Si}_2$ phase, the concentration of Mn was increased from 0.1 wt.% to 0.41 wt.% and the Mg was reduced from 0.49 wt.% to 0.25 wt.%. The following conclusions can be drawn from this study:

- (1) The thermodynamic simulations revealed that the modified chemistry had little effect on solidus and liquidus temperature of the alloys. The solidification range of FCC-Al increased by only 5–6 °C in the high Mn, low Mg alloy (i.e., A356RE-B). However, the Mn addition more than tripled the mass fraction of $\text{Al}_{15}(\text{Fe,Mn})_3\text{Si}_2$, while nearly halving the mass fraction of $\text{Al}_9\text{FeSi}_3\text{Mg}_5$ and Al_5FeSi . The total mass fraction of Fe phases in A356RE-B was nearly twice as large as reported for A356RE-A. The simulations also suggest that the mass fraction of the thermally stable RE-bearing intermetallics (i.e., $\text{Al}_4\text{Ce}_3\text{Si}_6$ and AlCeSi) are unaffected by the modified composition.
- (2) The results from SEM/EDS analysis somewhat closely match the simulated observations. The chemical modification led to a near complete transformation of the two harmful Fe phases into the more favorable $\text{Al}_{15}(\text{Fe,Mn})_3\text{Si}_2$ intermetallic. In addition, this transformation increased the area fraction of the Fe phases, leading to a greater contribution from Orowan strengthening. Lastly, it appears that the modified chemistry also partially transformed the size and shape of the elongated rod/plate-like structure of the AlSiRE phase into a smaller, faceted Chinese script style morphology.

- (3) The elevated temperature (250 °C) tensile tests of A356RE-A (high Mg, low Mn) and A356RE-B (low Mg, high Mn) alloys revealed that the chemistry modification markedly improved the tensile properties of the alloy system. Specifically, the YS, UTS, and modulus of elasticity improved by ~14%, 9%, and 10%, respectively. In addition, the elongation increased from 8.9% to 9.6%. The near complete transformation of $\text{Al}_9\text{FeSi}_3\text{Mg}_5$ and Al_5FeSi into $\text{Al}_{15}(\text{Fe,Mn})_3\text{Si}_2$, as well as the increased total area fraction of phases, are believed to be two of the primary factors contributing to the improved tensile performance of A356RE-B. In addition, the transformation of the elongated plate-like AlSiRE precipitates to the shorter and more interconnected Chinese script morphology is presumed to provide additional resistance to dislocation motion, thereby, further improving the alloy's strength.
- (4) In addition to improving the tensile properties of the A356RE-A alloy, the modified chemistry resulted in a considerable improvement in the alloy's creep resistance. The steady-state creep rate at all of the applied stresses was notably lower for A356RE-B than for A356RE-A. It should be noted that although the alloys both failed only when the applied stress reached ~100% of their measured YS, A356RE-B failed at a 10–15 MPa higher stress as compared to A356RE-A.
- (5) The chemistry modification lowered the apparent stress exponent at all stress intervals and increased the stress range at which diffusional creep is the dominant mechanism. Moreover, the threshold stress increased from 34.3 to 44.2 MPa, which is presumed to be attributed to the increased volume fraction of available precipitates for pinning dislocations.

The clear benefits attributed to the chemistry modification provide sufficient evidence that lowering the Mg and increasing the Mn concentrations can improve the alloy's elevated temperature tensile and creep performance with little to no additional costs for manufacturers.

Author Contributions: Conceptualization, J.S.; methodology, J.S. and D.W.; software, J.S.; validation, J.S.; formal analysis, J.S.; investigation, J.S. and D.W.; resources, D.S. and D.W.; data curation, J.S.; writing—original draft preparation, J.S.; writing—review and editing, D.S. and D.W.; visualization, J.S. and D.W.; supervision, D.S. and D.W.; project administration, D.S. and D.W.; funding acquisition, D.S. and D.W. All authors have read and agreed to the published version of the manuscript.

Funding: This work was supported by the Mitacs International Award [Application Ref. IT15556].

Data Availability Statement: The raw and processed data required to reproduce these findings are available to download from Mendeley Data ["Data for the Effects of Fe-phase on RE-modified A356 Alloy", doi:10.17632/fsjrsvsk68.1].

Acknowledgments: The authors would like to greatly acknowledge the financial support from Eck Industries and Mitacs.

Conflicts of Interest: David Weiss is an employee of Eck Industries Inc and is one of the inventors of the alloy system that is partially included in this work that is patented as US patent 9,963,700, Castable High Temperature Ce Modified Al Alloys.

References

1. Sims, Z.; Rios, O.; Weiss, D.; Turchi, P.; Perron, A.; Lee, J.T.; Li Hammons, J.; Hansen, M.; Wiley, T.; Chen, K.; et al. High performance aluminum-cerium alloys for high-temperature applications. *Mater. Horiz.* **2017**, *4*, 1070–1078. [[CrossRef](#)]
2. Stroh, J.; Sediako, D.; Weiss, D.; Peterson, V.K. In situ neutron diffraction solidification analyses of rare earth reinforced hypoeutectic and hypereutectic aluminum–silicon alloys. *Light Met.* **2020**, *2020*, 174–178.
3. Stroh, J.; Davis, T.; Mcdougal, A.; Sediako, D. In situ study of solidification kinetics of Al-Cu and Al-Ce-Mg alloys with application of neutron diffraction. *Light Met.* **2018**, *2018*, 1059–1065.
4. Stroh, J.; Sediako, D.; Weiss, D. Development of cerium-reinforced specialty aluminum alloy with application of x-ray and neutron diffraction. *Int. J. Met.* **2020**, *15*, 1–11.
5. Vogel, R. Cerium-aluminum alloys. *J. Franklin Inst.* **1912**, *174*, 342.
6. Buschow, K.; Vucht, J. The binary systems cerium-aluminum and praseodymium-aluminum. *Z. Met.* **1966**, *57*, 162–166.
7. Vucht, J. Contribution to the knowledge of the system of cerium-aluminum. *Z. Met.* **1957**, *48*, 252–258.

8. Gillett, H.W.; Schnee, V.H. Cerium in aluminium alloys. *Ind. Eng. Chem.* **1923**, *15*, 709–711. [CrossRef]
9. Langenbeck, S.L.; Griffith, W.M.; Hildeman, G.J.; Simon, J.W. Rapidly solidified powder aluminum alloys. In *Rapidly Solidified Powder Aluminum Alloys*; ASTM International: West Conshohocken, PA, USA, 1986; pp. 410–422.
10. Aghaie, E.; Stroh, J.; Sediako, D.; Rashidi, A.; Milani, A.S. Improving the mechanical properties of the B319 aluminum alloy by addition of cerium. *Mater. Sci. Eng. A* **2020**, *793*, 1–9. [CrossRef]
11. Jin, L.; Liu, K.; Chen, X.G. Evolution of dispersoids and their effects on elevated-temperature strength and creep resistance in Al-Si-Cu 319 cast alloys with Mn and Mo additions. *Mater. Sci. Eng. A* **2020**, *770*, 138554. [CrossRef]
12. Sims, Z.; Weiss, D.; Rios, O.; Henderson, H.; Kesler, M.; McCall, S.; Perron, A.; Moore, E. The efficacy of replacing metallic cerium in aluminum–cerium alloys with LREE mischmetal. *Light Met.* **2020**, *2020*, 216–221.
13. Weiss, D. Development and casting of high cerium content aluminum alloys. *Mod. Cast.* **2017**, *107*, 35–38.
14. Stroh, J.; Sediako, D.; Weiss, D. The effect of rare earth mischmetal on the high temperature tensile properties of an A356 aluminum alloy. *Light Met.* **2021**, *2021*, 184–191.
15. Lu, L.; Dahle, A.K. Iron-rich intermetallic phases and their role in casting defect formation in hypoeutectic Al-Si alloys. *Metall. Mater. Trans. A* **2005**, *36A*, 819–835.
16. Mbuya, T.O.; Odera, B.O.; Ng'ang'a, S.P. Influence of iron on castability and properties of aluminium silicon alloys: Literature review. *Int. J. Cast Met. Res.* **2003**, *16*, 451–465. [CrossRef]
17. Belov, N.; Aksenov, A.; Eskin, D. *Iron in Aluminum Alloys: Impurity and Alloying Element*; Taylor & Francis: London, UK, 2002.
18. Taylor, J.A. Iron-containing intermetallic phases in Al-Si based casting alloys. *Procedia Mater. Sci.* **2012**, *1*, 19–33. [CrossRef]
19. Dinnis, C.; Taylor, J. Porosity formation and eutectic growth in Al-Si-Cu-Mg alloys containing iron and manganese. *Mat. Sci.* **2004**, *2004*, 1016–1021.
20. ASTM. *E3-11 Standard Guide for Preparation of Metallographic Specimens 1*; ASTM Copyright; ASTM International: West Conshohocken, PA, USA, 2011; pp. 1–12.
21. Karlsruhe, F. Inorganic Crystals Structures Database; Leibniz Institutue for Information Infrastructure. 2020. Available online: <https://icsd.fiz-karlsruhe.de/search/basic.xhtml> (accessed on 20 September 2020).
22. ASTM. *E8M Standard Test Methods for Tension Testing Wrought and Cast Aluminum- and Magnesium-Alloy Products*; ASTM B. Standards: West Conshohocken, PA, USA, 2009; pp. 1–16.
23. Dieter, G.E. *Mechanical Metallurgy*, 3rd ed.; McGraw Hill Publishing Co.: Whitby, ON, Canada, 1986.
24. Sherby, O.D.; Burke, P.M. Mechanical behavior of crystalline solids at elevated temperature. *Prog. Mater. Sci.* **1968**, *13*, 323–390. [CrossRef]
25. Deshmukh, S.P.; Mishra, R.S.; Kendig, K.L. Creep behavior and threshold stress of an extruded Al-6Mg-2Sc-1Zr alloy. *Mater. Sci. Eng. A* **2004**, *381*, 381–385. [CrossRef]
26. Knipling, K.E.; Dunand, D.C. Creep resistance of cast and aged Al-0.1Zr and Al-0.1Zr-0.1Ti (at.%) alloys at 300–400 °C. *Scr. Mater.* **2008**, *59*, 387–390. [CrossRef]
27. Mitra, S. Elevated temperature deformation behavior of a dispersion-strengthened Al-Fe,V,Si alloy. *Metall. Mater. Trans. A Phys. Metall. Mater. Sci.* **1996**, *27A*, 3913–3923. [CrossRef]
28. Sherby, O.; Klundt, R.; Miller, A. Flow stress, subgrain size, and subgrain stability at elevated temperature. *Metall. Trans. A* **1977**, *8A*, 843–850. [CrossRef]
29. Marquis, E.A.; Dunand, D.C. Model for creep threshold stress in precipitation-strengthened alloys with coherent particles. *Scr. Mater.* **2002**, *47*, 503–508. [CrossRef]
30. Krug, M.E.; Dunand, D.C. Modeling the creep threshold stress due to climb of a dislocation in the stress field of a misfitting precipitate. *Acta Mater.* **2011**, *59*, 5125–5134. [CrossRef]
31. *Standard Test Methods for Conducting Creep, Creep-Rupture, and Stress-Rupture Tests of Metallic Materials*; ASTM E139-11; ASTM International: West Conshohocken, PA, USA, 2018; pp. 1–18.
32. Garat, M.; Laslaz, G. Improved aluminium alloys for common rail diesel cylinder heads. *Trans. Am. Foundry Soc.* **2007**, *115*, 1–8.
33. Farkoosh, R.; Pekguleryuz, M. The effects of manganese on the T-phase and creep resistance in Al-Si-Cu-Mg-Ni alloys. *Mater. Sci. Eng. A* **2013**, *582*, 248–256. [CrossRef]
34. Frost, H.J.; Ashby, M.F. *Deformation Mechanism Maps*; Oxford Pergamon Press: Oxford, UK, 1982.
35. Sato, E.; Takayama, Y.; Shibayanagi, T.; Kitazono, K. Re-Examination of Deformation Mechanism Map of Pure Aluminum. In Proceedings of the 12th International Conference on Aluminium Alloys, Yokohama, Japan, 5–9 September 2010; pp. 1559–1566.
36. Sediako, D.; Kasprzak, W.; Czerwinski, F.; Nabawy, A.; Farkoosh, A. High Temperature creep evolution in Al-Si alloys developed for automotive powertrain applications a neutron in-situ study on Hkl-plane creep response. *Light Met.* **2016**, *2016*, 131–136.
37. Hawksworth, A.; Rainforth, W.; Jones, H. Thermal stability of Al/Al11Ce3 and Al/Al11La3/Al3Ni eutectics obtained by Bridgman growth. *Mater. Sci. Technol.* **1999**, *15*, 616–620. [CrossRef]
38. Keyhani, R.R.; Mohammadi, S. An efficient computational technique for modeling dislocation-precipitate interactions within dislocation dynamics. *Comput. Mater. Sci.* **2016**, *122*, 281–287. [CrossRef]
39. Erfanian-Naziftoosi, H.R.; Rincón, E.J.; López, H.F. Creep properties of the As-Cast Al-A319 alloy: T4 and T7 heat treatment effects. *Metall. Mater. Trans. A* **2016**, *47A*, 4258–4267. [CrossRef]
40. Park, K.T.; Lavernia, E.J.; Mohamed, F.A. High-temperature deformation of 6061 Al. *Acta Metall. Mater.* **1992**, *42*, 667–678. [CrossRef]

-
41. Farkoosh, R. *Development of Creep-Resistant Al-Si Cast Alloys Strengthened with Nanoscale Dispersoids*; McGill University: Montreal, QC, Canada, 2014.
 42. Sediako, D.; Weiss, D.; Nabawy, A. Advanced aluminum alloy development and in-situ fitness-for-service testing for automotive lightweighting. *Light Met.* **2017**, *2017*, 639–644.